Near-infrared spectroscopy of the Antennae (NGC 4038/4039): properties of young super star clusters ⋆

Leonie Snijders[1] and Paul P. van der Werf[1]

Leiden Observatory, Leiden University, PO Box 9513, 2300 RA Leiden, The Netherlands
e-mail: `pvdwerf@strw.leidenuniv.nl`

Received; accepted

ABSTRACT

Context. Starburst galaxies produce the most massive star clusters known, with masses up to several million $M_\odot$. The work presented here is part of a larger study with the goal to gain a more detailed understanding of the nature of these so-called super star clusters, their stellar populations and the surrounding gas and dust in which they are formed.

Aims. The objective of this work is to accurately determine various properties of massive star-forming regions: the age of the stellar populations, the amount of extinction obscuring the star clusters, the present-day upper mass cutoff, the cluster masses and the density of the surrounding interstellar matter.

Methods. We obtained medium-resolution spectra in the J-, H-, K_s-band of the four brightest near-infrared peaks in the Antennae (NGC 4038/4039) overlap region. By comparing the continuum emission and the observed strength of the hydrogen recombination lines with predictions by models of embedded star clusters, we determine the cluster masses and ages. Furthermore, the density of the molecular gas is constrained by comparison of the observed ro-vibrational H_2 lines with results from models of photon-dominated regions (PDRs).

Results. The near-infrared spectra show the characteristic features of a recent episode of active star formation: strong H I and He I recombination lines (hydrogen Brackett series up to Br30), strong [Fe II] fine-structure lines and numerous ro-vibrational H_2 lines. Our models indicate that three of the four clusters are younger than 3 Myr. The fourth is somewhat older, 3 – 5 Myr, which is also apparent from the presence of (weak) CO bandheads in its K_s-band spectrum, indicating the presence of a somewhat more evolved stellar population. In the H-band we observe several high vibrational level (v = 3,4,5,6,7) H_2 emission lines. These lines have such high upper level temperatures (≥ 15,000K) that they can not be excited thermally, and thus reveal the presence of fluorescent UV-pumped H_2 emission.

Conclusions. The four clusters are all very young (5 Myr or younger) and very massive (two clusters have masses greater than a million $M_\odot$). The relative strength of the H_2 ratios strongly indicates that UV fluorescence in dense PDRs is an important excitation mechanism in all four star-forming regions. To explain the observed H_2 line ratios, the molecular gas densities have to fall in the range of several 10^4 to 1.5 times 10^5 cm^{-3}.

Key words. galaxies: individual (NGC 4038/4039) — galaxies: starburst, star clusters — ISM: HII regions — ISM: PDR — ISM: H_2 emission — infrared: ISM

1. Introduction

The Antennae galaxies (NGC 4038/4039) are the most striking nearby examples of a major merger in action. The initial encounter took place approximately 210 Myr ago and simulations indicate that these two giant spirals will eventually merge into a elliptical-like galaxy (Mihos et al, 1993). Triggered by the encounter vigorous bursts of star formation took and still take place across the system, resulting in numerous massive star clusters (Whitmore & Schweizer, 1995). Most of these are young, bright, intrinsically very blue stellar populations, but clusters with an age of several hundreds Myrs, probably formed during the first fly-by, can be identified as well (Whitmore et al., 1999).

Observations from Infrared Space Observatory (ISO) revealed the region where the two spirals overlap as the location of most recent (or even still on-going) star formation. In ISO's mid-IR images the NGC 4038 and NGC 4039 nuclei are not the brightest sources in the Antennae. Hidden from view at shorter wavelengths by massive amounts of dust, the most active region of star formation located in the overlap region outshines all other sources (Vigroux et al., 1996; Mirabel et al, 1998). This source, which is only ~100 pc in diameter (from ground-based N-band observations, Snijders et al, 2006), is solely responsible for 15% of all 15 μm emission from the Antennae. After its initial discovery, this star cluster has been studied extensively. The cluster is highly obscured (A_V = 4.2 – 10), very young (< 2.5 Myr), very massive (several million solar masses), and it resides in a high pressure environment (ionized gas density ≥ 10^4 cm^{-3}; Whitmore & Schweizer, 1995; Whitmore et al., 1999; Gilbert et al, 2000; Mengel et al, 2001, 2005; Snijders et al, 2006; Gilbert & Graham, 2007; Snijders et al, 2007). Close to this extremely bright and massive cluster, several other super star cluster (with masses $\gtrsim 10^6 M_\odot$) can be found in the overlap region.

One of the important questions is whether these stellar populations are and will stay gravitationally bound to form stable, long-lived, massive star clusters, like the globulars observed in our own Milky Way and other nearby galaxies. Observational evidence exists that most clusters in the Antennae disperse on a

---

Send offprint requests to: Paul van der Werf

⋆ Based on observations collected at the European Southern Observatory, Paranal, Chile, under programme no. 68.A-0243(A) and 69.B-0688(A) timescale of ~ 10 Myr (infant mortality; Fall et al, 2005; Mengel et al, 2005; Gilbert & Graham, 2007). To be able to answer this question we need to gain detailed knowledge of the stellar population, its stellar content, age, mass, and morphology, and of the characteristics and the geometry of the surrounding gas and dust. Determination of these various properties are the main goal of this work.

As already shown by ISO, observations at longer (infrared) wavelengths are crucial in identifying and studying the star formation in these dusty system, specially since we are interested in the youngest, most massive, and thus most deeply embedded star clusters. So, we obtained near-IR medium-resolution spectroscopy with the Infrared Spectrometer And Array Camera (ISAAC, Moorwood et al, 1998) at the Very Large Telescope (VLT). In these J-, H-, and K_s-band spectra many features are available to study the physical characteristics of the star cluster and the surrounding ISM. Originating from the H II region directly around the cluster, strong H I and He I recombination lines excited by massive O and B stars can be found. Further out from the cluster, molecular hydrogen residing in the photon dominated region (PDR) can be observed through rotational-vibrational H_2 emission lines. Direct starlight combined with nebular emission makes up the near-infrared continuum.

In Section 2 the observations and data reduction are discussed, and a description of the results can be found in Section 3. In Section 4 the derived properties of the stellar populations are presented. Section 5 deals with the excitation mechanism of the ro-vibrational H_2 lines. Lastly, the conclusions can be found in Section 6.

2. Observations and data reduction

Medium-resolution spectra in the J-, H-, and K_s-band were obtained of the four brightest near-IR peaks in the Antennae overlap region using ISAAC in February, April and May 2002. The location of these four targets can be found in Fig. 1. In Table 1 the exact positions and optical and near-IR counterparts are listed. The first source, cluster 1, is the brightest mid-IR peak of the Antennae (source 1a in Snijders et al, 2006). In the optical a faint, highly reddened source can be identified at the same location, [WS95]80 (source 80 in Whitmore & Schweizer, 1995, WS95 hereafter). Cluster 2 coincides with a bright blue cluster complex in the optical images ([WS95]86 – 90, and the mid-IR source 2 in Snijders et al, 2006). For cluster 3 multiple possible counterparts are identified as well, [WS95]119, [WS95]120, and [WS95]117. Lastly, cluster 4 corresponds to one of the reddest sources in the Antennae, [WS95]115 in the HST images. Additionally, two of these sources (cluster 1 and 2), were observed in a medium-resolution L-band spectroscopic setting around the hydrogen Brα recombination line (at 4.0523 μm). With a 1″ slit the medium-resolution mode provides a resolution of 3100 (J), 3000 (H, L) and 2600 (K_s). Given the detector's spectral coverage at these resolutions, it takes several settings with varying central wavelength to cover a full near-IR band. The J-band was only partly observed; one spectral setting was chosen to cover both the hydrogen Paβ (1.2822 μm) and the [Fe II] (1.2572 μm) emission lines (central wavelength of the setting was 1.27(5) μm). The H- and K_s-band were almost fully observed, each in 4 or 5 settings. The seeing varied from 0.″8 to 1.″3 during the observations.

Chopping and nodding along the slit was applied with a chop throw of 30″. Given the pixel scale of 0.″148/pix, the detector's coverage is 152″in the spatial direction, which is large enough to have both the positive and negative beam on the detector. The total integration time was 20 minutes for each spectroscopic setting in J-, H- and K_s-band and 80 seconds in L-band. Before or after the science target observations, B2, B3, and B5 stars (and one G2 star) were observed near the target to provide telluric standards at similar airmass (Hip052670, Hip053690, Hip058587, Hip065630, Hip075577, Hip087287, and Hip095652).

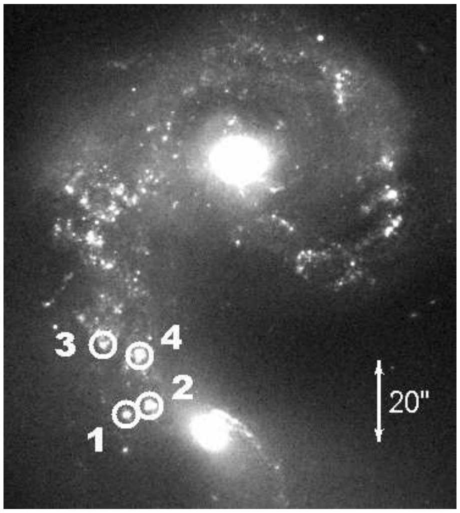

Fig. 1. ISAAC K_s-band image of NGC 4038/49 kindly provided by S. Mengel, with the positions of the observed clusters indicated (North is up and East to the left). The two brightest areas are the original premerger nuclei, the northern one is NGC 4038 and the southern NGC 4039.

After removal of bad pixels and cosmic rays (using the IRAF procedure xzap), the two-dimensional spectra were reduced using *Eclipse v.4.9.0* (Devillard, 1997). The resulting nonlinearity-corrected, flat-fielded, sky-subtracted and curvature-corrected frames were processed further using IRAF routines and customized scripts. The spectra were extracted in 3.″5 and 5.″1 apertures (which corresponds to ~370 and 535 pc respectively at a distance of 21 Mpc[1], assuming a Hubble constant of 70 km s^{-1} Mpc^{-1}; at this distance 1″ corresponds to 105 pc). The 3.″5 aperture covers the continuum and the ionized gas emission. The larger aperture contains the more extended line emission from molecular hydrogen and iron as well. Wavelength calibration was applied to the extracted spectra using atmospheric OH lines or, when the OH lines where too weak (at the long wavelength end of the K_s-band), using lines from xenon and argon lamps. To correct for atmospheric transmission, the wavelength calibrated spectra were divided by the B star calibration spectra. The reduction procedure for these standard star spectra was identical to that for the science frames, with the additional step of removing the few stellar absorption features present in the spectra. The resulting calibration spectra were divided by a black-body curve of the appropriate temperature to compensate for the continuum shape of the standard star. Finally, flux calibration was performed by normalization to the broad-band fluxes of the calibration stars (from the Hipparcos Catalogue, Perryman et al, 1997).

---

[1] Note that the distance of the Antennae is under debate. Recently a lower distance of 13.8 ± 1.7 Mpc was found (Saviane et al, 2004), which would affect the values derived here.

3. Results

The spectra of all four sources show clear signatures of recent star formation (Figs. 3 and 4): strong hydrogen and helium recombination lines from the H ii region surrounding the star cluster, strong [Fe ii] fine-structure lines, revealing shocked gas from recent supernovae, and a number of ro-vibrational H_2 lines, originating from warm gas in the PDR. The weakness of the CO absorption bandheads in the K_s-band shows that the emission is dominated by very young stellar populations. Red super giants do not play an important role yet, so these clusters must all be younger than ∼7 Myr (Leitherer et al, 1999)

Line fluxes were measured with ISAP[2]. For each emission line a linear fit to the local continuum was subtracted. The line flux was calculated by integrating over a gaussian fit to the continuum-subtracted emission line. In case of blending, the lines were fitted simultaneously. All H i, He i, and [Fe iii] lines, were measured from the spectra extracted in the 3″.5 aperture. The H_2 and [Fe ii] lines are more extended than 3″.5, and are measured from the spectra extracted in a 5″.1 aperture. The spectral calibration is accurate to 0.0006 μm, which is about one resolution element. Faint emission lines are identified using the wavelength-offset relative to bright lines with undisputed identifications (e.g. from the Brackett series). The resulting line fluxes are listed in Table 2.

4. Cluster properties

To derive various properties of the stellar populations we use the results of Snijders et al (2007, SKW07 hereafter). In that paper the evolution of the near- and mid-IR spectral energy distributions (SEDs) of young, embedded star clusters is modeled. The stellar populations plus their surrounding ISM are modeled by combining synthesized SEDs from the stellar population code *Starburst 99 v5.1* (Leitherer et al, 1999; Vázquez & Leitherer, 2005) with the photoionization code *Mappings IIIr* (Dopita et al, 2000, 2002; Groves, Dopita & Sutherland, 2004). The age evolution of a one million $M_\odot$ star cluster, formed in an instantaneous burst with a Salpeter IMF between 0.1 and 100 $M_\odot$, is modeled for various values of metallicity, ionized gas density and of the characteristic ionization parameter of the surrounding dusty nebula. The SEDs are evaluated from 0 – 6 Myr, for 0.4, 1 and $2Z_\odot$. The ionized gas density is varied from 10^2 to 10^6 cm^{-3}. The ionization parameter q is defined as $q = Q_{Lyc}/4\pi R^2 n_{ion}$, with Q_{Lyc} the hydrogen ionizing photon flux, R the distance between the radiating source and the inner boundary of the surrounding cloud, and n_{ion} the gas density. The ionization parameter ranges from $2 \cdot 10^7$ cm s^{-1} to $8 \cdot 10^8$ cm s^{-1}. It relates to the commonly used dimensionless ionization parameter U through $U \equiv 1.1 \cdot q/c$, where the factor 1.1 takes the helium abundance into account (for a more detailed description and examples of the resulting model SEDs, see SKW07).

4.1. Extinction

To determine the extinction that is affecting the measurements of the H ii region, we use Paβ in the J-band and all lines of the Brackett series with sufficient signal-to-noise in the H- and K_s-band (plus Brα in the L-band for cluster 1 and 2). From the observed ratios of each of these hydrogen lines relative to Brγ we derive the attenuation factors by least-squares fitting both the case of a foreground screen of extinction as well as the case in which the obscuring matter is mixed with the cluster stars. The intrinsic hydrogen line ratios were obtained from Hummer & Storey (1987) for case B recombination with T_e = 10,000 K and $n_e = 10^4$ cm^{-3} (consistent with ionized gas densities $\geq 10^4$ cm^{-3} derived from mid-IR fine-structure lines, SKW07). We use the reddening curve presented in Draine (1989). The geometry of a foreground screen of obscuring material provides a much better fit than the mixed morphology (having a significantly smaller χ-squared value), so in further analysis we will use extinction values derived by fitting a foreground screen (see values for A_V in Table 1)

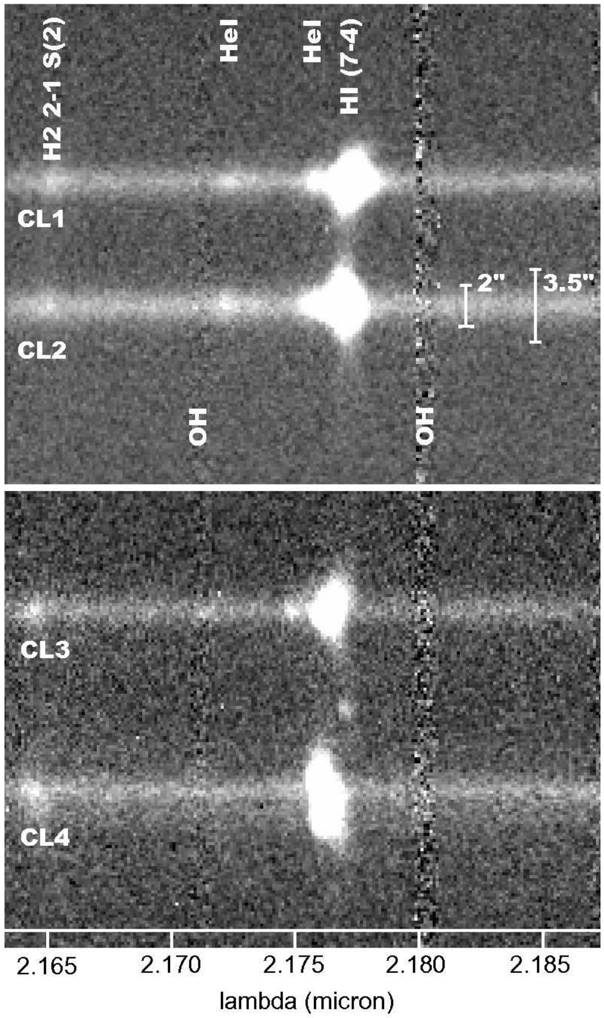

Fig. 2. The 2D K_s-band spectra between 2.163 – 2.188 μm for all four clusters. The wavelength axis is horizontal and the spatial axis is vertical. The Brγ emission is clearly more extended than the continuum emission. The aperture sizes indicated in the top plot show that a 3″.5 is required to cover the Brγ emission.

4.2. Cluster ages

Under the assumption that the near-IR radiation is dominated by stars formed in a single bust of star formation, the equivalent width (EW) of the hydrogen recombination lines can be used to estimate the age of the star cluster. The hydrogen lines rapidly weaken during the first 10 Myr. The underlying near-IR

---

[2] The ISO Spectral Analysis Package is a joint development by the LWS and SWS Instrument Teams and Data Centers. Contributing institutes are CESR, IAS, IPAC, MPE, RAL and SRON.

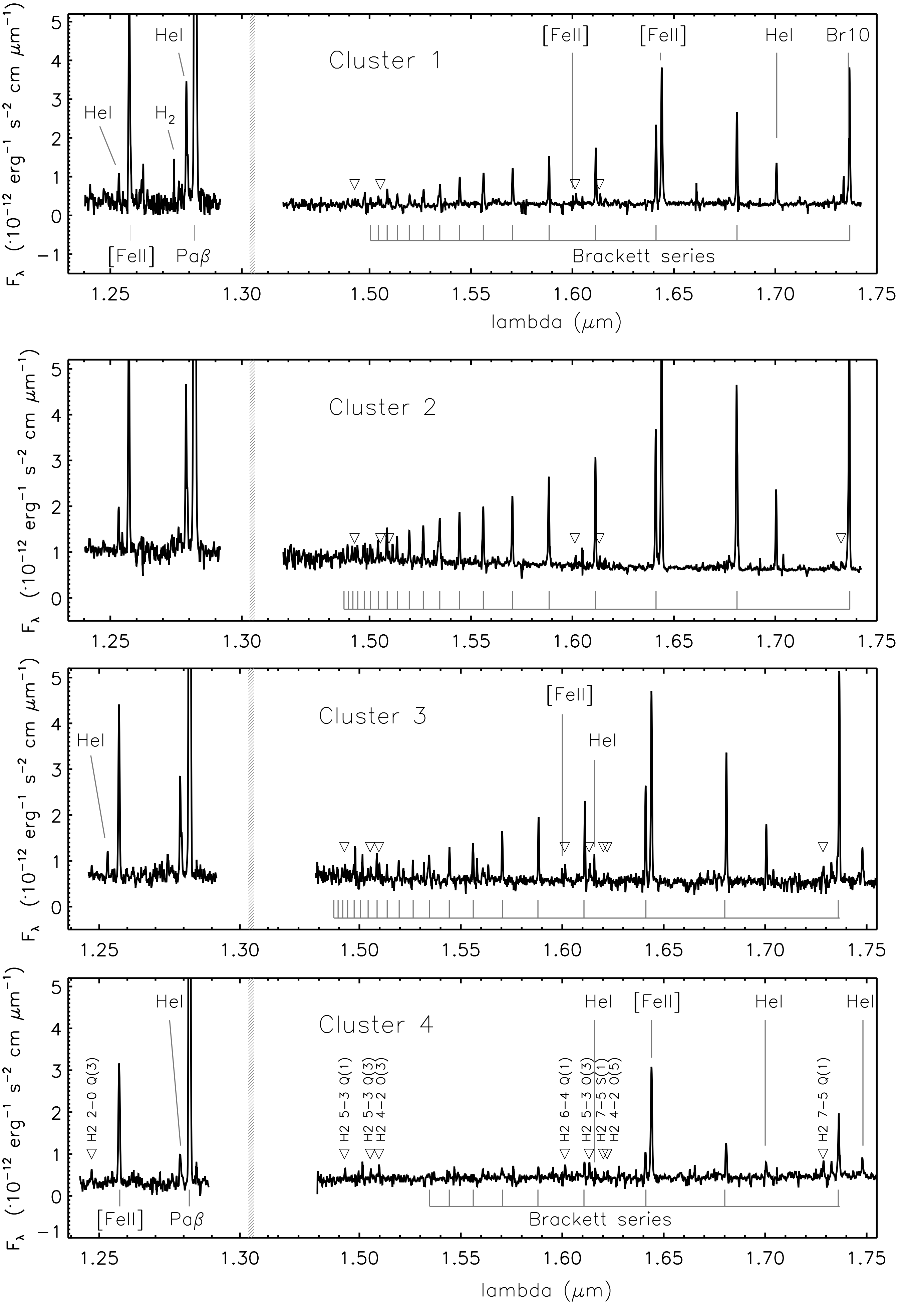

Fig. 3. Medium-resolution J- and H-band spectra with various emission lines labeled. The wavelengths of the H I recombination lines from the Brackett series are indicated below the H-band spectra. H_2 ro-vibrational lines are marked with triangles, which are labeled in the spectrum of cluster 4. In the other three spectra, only triangles are shown.

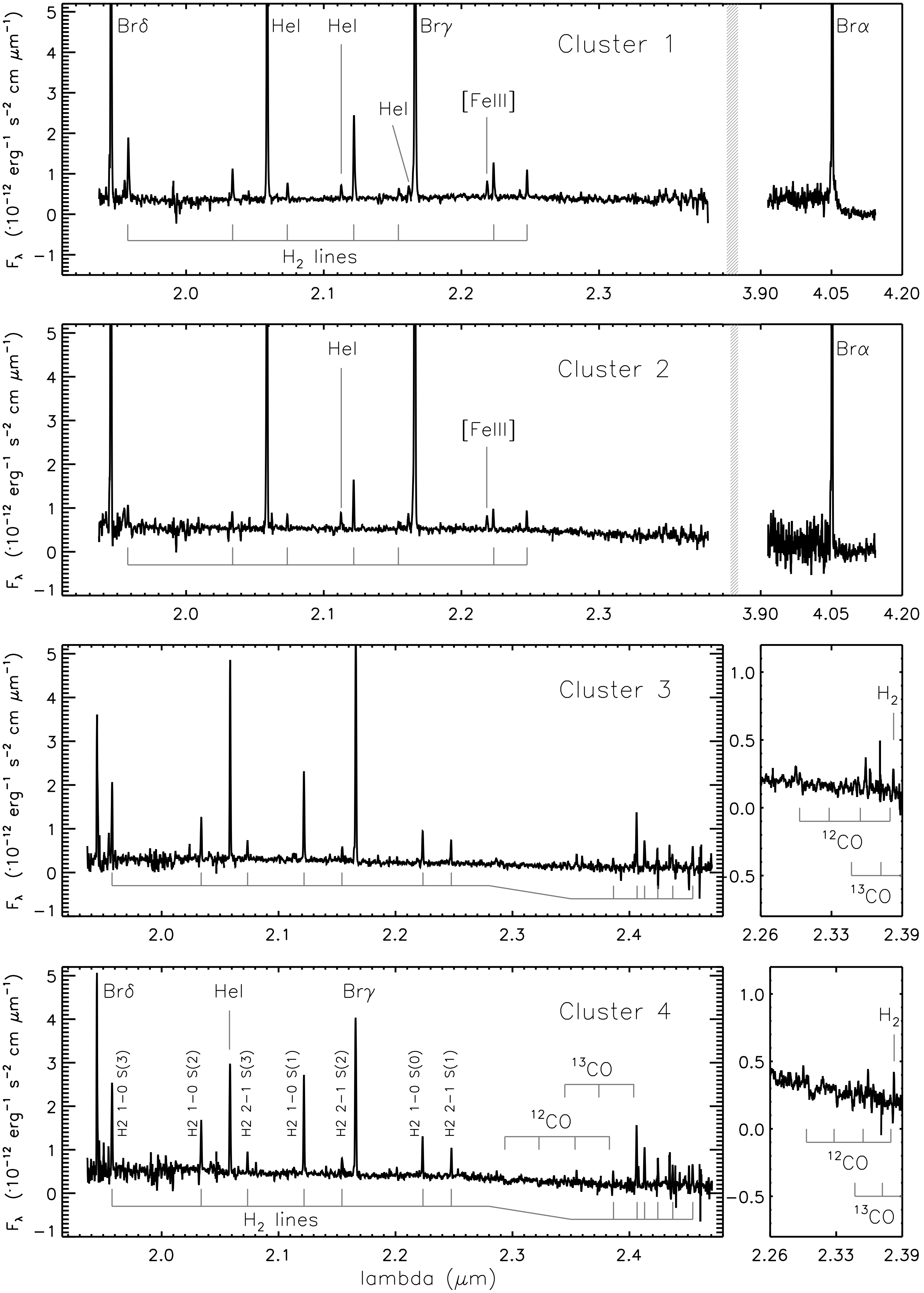

Fig. 4. Medium-resolution K_s-band spectra. For cluster 1 and 2 the right hand panel shows L-band medium-resolution spectroscopy. For cluster 3 and 4 a blow-up of the spectral range around the CO bandheads is added. The wavelengths of the H_2 ro-vibrational lines are indicated below the K_s-band spectra and labeled in the spectrum of cluster 4. Furthermore, the location of several ^{12}CO and ^{13}CO bandheads are indicated in the bottom panel.

Table 1. Properties of the star clusters.

#	RA[a]	DEC[a]	[WS95]#[b]	ID_{WIRC}[c]	A_V (mag)	T_{eff} (10^3 K)	Age (Myr)	Mass[d] (10^6 $M_\odot$)
1	12:01:54.96	-18:53:06.2	80	157	6.2 ± 0.3	≥38.0	0 – 2.5	1.1 – 1.2
2	12:01:54.54	-18:53:04.0	86/87/88/89/90	136	0.7 ± 0.1	$39.0^{+1.0}_{-2.0}$	0 – 3	1.2 – 1.7
3	12:01:55.36	-18:52:49.2	119/120/117	176	4.8 ± 0.4	$37.0^{+0.5}_{-1.0}$	1 – 3	0.1 – 2.4
4	12:01:54.75	-18:52:51.7	115	148	10.3 ± 0.5	≥39.0	3 – 5	0.1 – 2.9

[a] Positions are obtained from a SOFI K_s broad-band image.
[b] From Whitmore & Schweizer (1995).
[c] From Brandl et al. (2005).
[d] The errors given are the fit errors given a Salpeter IMF between 0.1 – 100 $M_\odot$. A different IMF would change the masses derived here.

continuum is dominated by less massive stars. To estimate the age of the Antennae star clusters we use model predictions for the EW(Brγ) (see Fig.7 in SKW07). In Fig. 5 the values measured for the EW(Brγ) for all four clusters are compared with the model predictions. Only the curves for solar metallicity are shown, although the 0.4 and 2$Z_\odot$ models are taken into account in the analysis. The derived ages are listed in Table 1.

Cluster 1 has the highest value for EW(Brγ) and is 2.5 Myr or younger. This is consistent with the results of Mengel et al (2005), 2.3 – 4.0 Myr. It is significantly lower than the age of 3.5 ± 0.1 Myr found by Gilbert & Graham (2007).

Cluster 2 is age-dated ≤ 3 Myr as well, in agreement with, although somewhat younger than the age found by Mengel et al (2005) (2.3 – 4.0 Myr).

Cluster 3 is very young as well, 3 Myr or less. This is consistent with the absence of significant CO bandheads in its K_s-band spectrum. Mengel et al (2005) estimated the age for cluster 3 to be somewhat older, 3.2 – 4.9 Myr. Results from Gilbert & Graham (2007) indicate a higher age as well, 3.9 ± 0.1 Myr. In both papers the age was determined from EW(Brγ), which was obtained from the combination of broad- and narrow-band imaging (K_s and the Brγ narrow-band filter Mengel et al, 2005) and from the combination of high-resolution spectroscopy of Brγ (no continuum detected) with K narrow-band imaging (Gilbert & Graham, 2007). Aperture effects are most probably responsible for the difference between the age estimates. Mengel and Gilbert use an aperture of 2.″2 and 2.″0 diameter respectively. From our spectra we know that the continuum indeed originates from a region smaller than 2″in size. However, the Brγ line emission is more extended with significant emission outside the central 2.″0 (see Fig. 2). Since the Brγ emission is centred on the continuum emission and there is no other source available for the excitation of the H II region than the clusters under study, we conclude that all Brγ emission (and that of all other hydrogen recombination lines as well) is associated with the central clusters. For this reason we chose the larger aperture of 3.″5, which results in a higher EW(Brγ) and thus a lower age than Mengel and Gilbert find.

Cluster 4 has the lowest value for the EW(Brγ), 114 ± 11Å. Almost all model curves for the age evolution of EW(Brγ) have an initial plateau at ~300 Å during the first 3 Myr, which is followed by a steep decline between 3 and 6 Myr. However, when both the ionization parameter and the gas density are very high ($q = 8 \cdot 10^8$ cm s^{-1}, $n_{ion} = 10^6$ cm^{-3}), the dust competes successfully with the gas for FUV photons, resulting in a lower value for the EW(Brγ) during the first 3 Myr (see long-dashed curves in the right panels in Fig. 5). This means that cluster 4 can essentially have any age in the range of 0 – 5 Myr, but an age < 3 Myr can only occur in combination with very extreme properties of the surrounding ISM. Since the density of the ionized gas in cluster 1 and 2 is derived to be ~10^4 cm^{-3} (Snijders et al, 2007), we do not expect cluster 4, which is generally thought to be located in a less active part of the overlap region, to be surrounded by gas two orders of magnitude denser. So, for cluster 4 the 10^6 cm^{-3} curve (long-dashed) in the lower right panel of Fig. 1 is ignored and we conclude that the age must lie in the range of 3 – 5 Myr. A lower age (< 3 Myr) would be inconsistent with the presence of the CO bandheads in the spectrum as well. These absorption features indicate an age close to the red super giant phase. Our age estimate agrees well with the age range of 3.7 – 5.1 Myr found by Mengel et al (2005). Gilbert & Graham (2007) again find a higher age, 5.7 ± 0.1 Myr.

The observed values of the line ratio [Fe II]$_{1.64\mu m}$/Brγ confirm the spread in cluster ages. First of all, the observed values for [Fe II]$_{1.64\mu m}$/Brγ are considerably higher than typical values for purely photoionized gas. In our sources [Fe II]$_{1.64\mu m}$/Brγ spans the range of 1.8 – 6.4, while a value of 0.06 is observed in the Orion Nebula (Lowe et al, 1979). Depending on the characteristics of the stellar population and the nebula the SKW07 models predict values of $4 \cdot 10^{-3} - 5 \cdot 10^{-1}$ for this line ratio in case of photoionization, significantly lower than the values observed. This means that shocks from super nova remnants (SNRs) are most probably the dominant excitation mechanism for the [Fe II] lines. In that case the value for [Fe II]$_{1.64\mu m}$/Brγ is expected to increase with cluster age, due to the increase in the number of SNRs and the decrease of FUV photons originating from massive, short-lived O stars. Cluster 1, 2 and 3 have similar values for [Fe II]$_{1.64\mu m}$/Brγ (1.9 ± 0.3, 1.8 ± 0.3 and 2.3 ± 0.3 respectively), which is ~3 times smaller than the ratio value observed in cluster 4 (6.4 ± 0.9). This strongly indicates that cluster 4 is considerably older than the other three clusters, and it shows that our assumption to ignore the option that cluster 4 is very young (< 3 Myr) is reasonable.

4.3. T_{eff} of the stellar radiation field

The value of He I$_{1.70\mu m}$/Br10 is a good indicator of the temperature of the radiation field. If the radiation is relatively soft, many photons are available in the range of 13.6 – 24.6 eV, capable of ionizing hydrogen but not helium. Photons with energies above the helium ionization boundary (> 24.6 eV) are scarce. This results in weak He I recombination lines relative to the H I lines. With an increasingly hard radiation field the helium Strömgren sphere gradually fills that of hydrogen, resulting in an increasing He I$_{1.70\mu m}$/Br10 ratio. When both the He I and

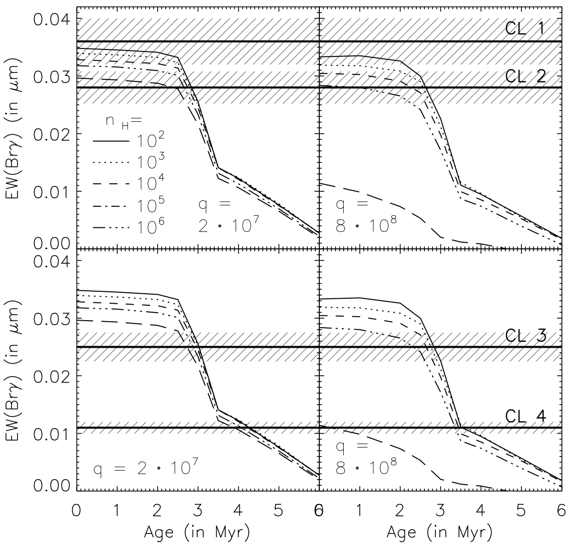

Fig. 5. Age evolution of the equivalent width of the hydrogen recombination line Brγ. All curves shown are for solar metallicity. The top panels show the measurements for clusters 1 and 2 (CL1 and CL2), and the bottom panels for clusters 3 and 4 (CL3 and CL4). The left panels show the case for low ionization parameter, $q = 2 \cdot 10^7$ cm s^{-1}, and the right panels that of high ionization parameter, $q = 8 \cdot 10^8$ cm s^{-1}. Curves of different line styles represent results of models with different densities, ranging from 10^2 cm^{-3} (solid line, upper curve) to 10^6 cm^{-3} (long-dashed line, lower curve). Curves for 0.4 and 2Z$_\odot$are not shown, but they are taken into account in the age estimate. However, the resulting ages for low or high metallicity do not alter the age ranges derived from Z$_\odot$ models. Line ratio values can be found tabulated at www.ifa.hawaii.edu/˜kewley/Mappings/IRdiagnostics

H I Strömgren spheres are maximally filled, the ratio value saturates. This mechanism makes the He I$_{1.70\mu\mathrm{m}}$/Br10 very sensitive to the effective temperature between 30,000K and 40,000K (bottom panel of Fig. 8 in Förster Schreiber et al, 2001, , who's results are consistent with those of SKW07).

In Fig. 6 the age evolution of He I$_{1.70\mu\mathrm{m}}$/Br10 is plotted as a function of metallicity and gas density. As the most massive stars disappear from the main-sequence, the cluster's FUV radiation softens and the He I/Br10 ratio drops. At 2.5 – 3 Myr (depending on metallicity) the first Wolf-Rayet (W-R) stars appear, hardening the radiation field and causing an upturn in the He I/Br10 line ratio. When the last W-R stars disappear at 4 – 6 Myr (again Z-dependent) the FUV field is dominated by O8 or later type stars. At this stage there are not many photons energetic enough to excite He I and the He I/Br10 ratio decreases to the point where He I lines are not observable anymore.

The extinction-corrected He I$_{1.70\mu\mathrm{m}}$/Br10 ratios are 0.32 ± 0.04, 0.30 ± 0.03, 0.24 ± 0.04, and 0.34 ± 0.05 for clusters 1, 2, 3, and 4 respectively (plotted in Fig. 6). The corresponding values for T$_{\mathrm{eff}}$ derived from Fig. 8 in Förster Schreiber et al (2001) are all 37,000 or higher (for clusters 1 and 4 only lower limits can be given, since the observed value reaches the saturated regime. See Table 1). We argued in Section 4.2 that cluster 4 is the oldest of the four clusters (3 – 5 Myr). The high value for He I$_{1.70\mu\mathrm{m}}$/Br10 measured in the spectrum of this cluster is thus an indication of the presence of W-R stars, which can easily reach temperatures $\gtrsim$ 40,000K (Woosley et al, 1993, and references therein). The He I$_{1.70\mu\mathrm{m}}$/Br10 values measured for cluster 1 and 2 are consistent with the low ages derived in the previous section. The lowest ratio value is observed for cluster 3. In this case the He I$_{1.70\mu\mathrm{m}}$/Br10 ratio can actually help to constrain the age further. Taking the error bars into account, cluster 3 must be older than 1 Myr, which narrows the age range for this cluster down to 1 – 3 Myr.

If the stellar populations of cluster 1, 2, and 3 are young enough to be pre-W-R-phase, the radiation temperature is still dominated by main-sequence stars. The most massive star present would then be a star of O6 or earlier spectral type for clusters 1 and 3, and an O6.5 or earlier type star for cluster 2 (using O star calibrations from Martins et al, 2005). However, we can not rule out the presence of W-R stars, since all clusters are possibly old enough for the first W-R stars to have appeared.

4.4. Cluster masses

Cluster masses were determined by fitting model SEDs to the extinction-corrected K$_s$-band spectra of the clusters. From the full model grid, all SEDs with an EW(Brγ) within 10% of the observed value were selected for each cluster (e.g. models within the correct age range). These selected model SEDs were scaled to the total K$_s$-band flux. Most of the model spectra have spectral slopes very similar to those observed. A handful of models however, the ones with very high ionization parameter and very high density already discussed in Section 4.2, have rising instead of downward slopes. In these high density cases, the dust absorbs many FUV photons and gets heated to such high temperatures that its thermal emission emission makes a significant contribution to the K$_s$-band continuum. These model spectra with clearly incorrect spectral shapes were not considered further. For the resulting subset of model spectra, which all obey the observational constraints, a cluster mass was derived for each individual model SED, resulting in a range in possible *initial* cluster masses (the cluster masses as they were at 0 Myr) for each source . The initial cluster mass was determined by dividing the total luminosity of the scaled model SEDs by the total luminosity for a one million M$_\odot$ mass cluster of the appropriate age as tabulated in the output of *Starburst 99*.

Unfortunately, for cluster 3 and 4 there are no further constraints (on for example the gas density or the ionization parameter), which can narrow down the set of suitable model SEDs. So for these two clusters this method results in a rather inconclusive mass range, from 100,000 M$_\odot$ up to almost 3 million M$_\odot$. These results are not extremely sensitive to the model parameters, but show a rough trend from high density and low ionization parameter for the low masses (n$_H \geq 10^5$ cm^{-3}, q $\leq 8 \cdot 10^7$ cm s^{-1}), to low density and high ionization parameters for the higher mass outcomes (n$_H \leq 10^3$ cm^{-3}, q $\geq 1.6 \cdot 10^8$ cm s^{-1}).

For clusters 1 and 2 constraints on the gas density and ionization parameter are available (SKW07). For these two stellar populations we only consider the model spectra with a gas density $\geq 10^4$ cm^{-3} and an ionization parameter q $\geq 4 \cdot 10^8$ cm s^{-1}. In this way a much tighter range of possible initial cluster masses is found; 1.1 – 1.2 million M$_\odot$ for cluster 1 and 1.2 – 1.7 million M$_\odot$ for cluster 2.

The mass range derived for cluster 2 is consistent with the mass derived by Mengel et al (2001), which is $1.6^{+1.2}_{-0.2} \cdot 10^6$ M$_\odot$. In that paper a Salpeter IMF between 1 – 100 M$_\odot$is adopted. The effect of the somewhat higher age they find for cluster 2 ($3.7^{+1.0}_{-0.4}$ Myr; leading to a higher initial mass) and the higher M$_{\mathrm{low}}$ (1 M$_\odot$; resulting in a lower initial mass) apparently cancel each other out. The mass for cluster 1 found by Gilbert & Graham (2007) is much higher, 5.0 ± 0.1 · 10^6 M$_\odot$. This is probably caused by the higher age they find for this source, 3.4 ± 0.1 Myr.

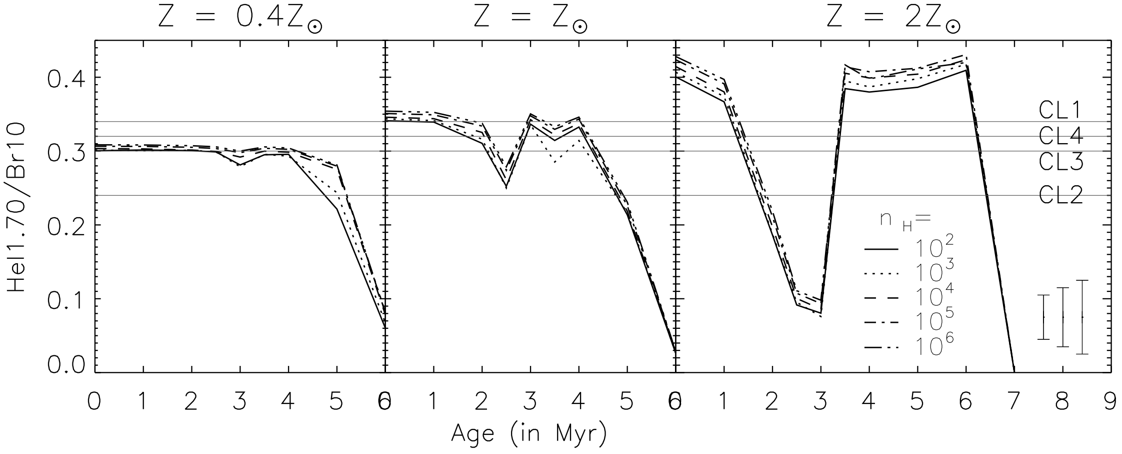

Fig. 6. Evolution of the He $\textsc{i}_{1.70\mu m}$/Br10 emission line ratio with cluster age. The left panels show the curves for $0.4Z_\odot$, the middle panels for $Z_\odot$ and the right panels for $2Z_\odot$. Curves of different line style represent results of models with different densities, ranging from 10^2 cm^{-3} (solid line) to 10^6 cm^{-3} (long-dashed line). The He $\textsc{i}_{1.70\mu m}$/Br10 ratio is hardly sensitive to the ionization parameter q (see SKW07). All curves shown here can be characterized by a q of $8 \cdot 10^8$ cm s^{-1}, which is an appropriate value for clusters 1 and 2 (derived in SKW07). Over-plotted are the observed extinction-corrected ratios for cluster 1, 2, 3, and 4 (CL1, CL2, CL3, and CL4 respectively). The error bars are given in the lower right panel for cluster 3 (leftmost error bar), cluster 2 (middle error bar), and cluster 1 and 4 (rightmost error bar). Line ratio values predicted by the models can be found tabulated at www.ifa.hawaii.edu/˜kewley/Mappings/IRdiagnostics.

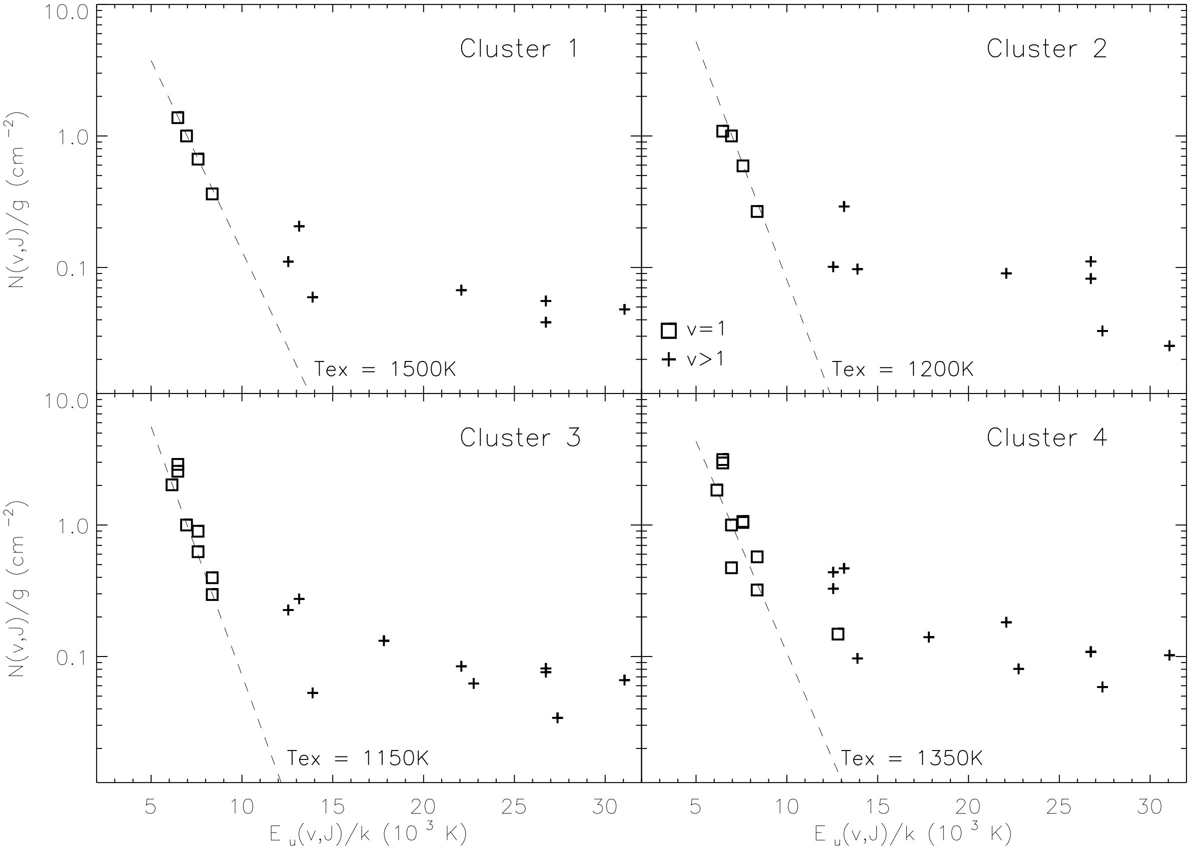

Fig. 7. Excitation diagrams of the H_2 level column density distribution as a function of level energy. The data points are extinction-corrected and normalized to the column density of the H_2 1-0 S(1) line. The squares represent al ro-vibrational lines from the v = 1 level, the plusses those originating from higher vibrational levels. The error bars are not plotted, they are generally smaller than the size of the symbols. The dashed line shows the expected values for thermally excited gas. The excitation temperature Tex represents the temperature of the best fitting Boltzmann distribution to the v = 1 data points.

The mass range found for cluster 1 is a factor of 3 – 4 lower than published values ($3.0^{+3.6}_{-0.7}$ and ~4.2 ± 0.1 · 10^6 $M_\odot$ Mengel et al, 2001; Gilbert & Graham, 2007). In both papers a significantly higher age is found for this cluster ($5.5^{+0.7}_{-0.8}$ and 3.5 ± 0.1 Myr in Mengel et al, 2001, and Gilbert et al, 2000, respectively), resulting in a higher initial mass. And again, different IMFs are applied.

The comparison of the results for the cluster masses of various authors shows that photometric masses are very sensitive to age, and totally dependent of the assumed IMF. Dynamical masses would give a much more robust result. However, due to the lack of absorption lines in the spectra of these very young star clusters, velocity dispersions are impossible to obtain. Our analysis indicate cluster masses in the same range as the masses determined for globular clusters, but it is unclear whether these systems are gravitationally bound and if they will survive the phase infant mortality observed to take place on a timescale of ~10 Myr in the Antennae (Fall et al, 2005; Mengel et al, 2005; Gilbert & Graham, 2007). To answer this question better constraints on the cluster masses and sizes are required. The sizes can be obtained using adaptive optics systems, but measuring accurate velocity dispersions will remain very difficult.

5. The excitation mechanism of molecular hydrogen

The near-IR H- and K_s-band are rich in ro-vibrational H_2 lines, which are generally strong in star-forming regions. These emission lines can be excited by UV emission from O and B stars, and/or thermally, like in shock-heated molecular gas (e.g. from supernovae, stellar outflows, or from colliding molecular clouds in a merger event). Both physical processes will leave their own distinct fingerprint on the relative strength of the H_2 lines. Absorption of a FUV-photon excites the H_2 molecule to an upper electronic state, which is followed by a fluorescent cascade down to the ground state, populating the various ro-vibrational energy levels 'top-down'. In shock-excited regions, the level populations are thermalized, populating the energy levels 'bottom-up'. Typically, the temperature of gas heated by shocks is a few 1000K. These temperatures are not high enough to result in a significant population of the higher energy ro-vibrational level ($v \geq 3$), which have upper energy levels $E(v, J)/k$ higher than 15,000K. The H_2 line ratios can thus be used to discriminate between these two physical processes.

Being amongst the brightest of all near-IR H_2 lines, the ratio between the H_2 2-1 S(1) (2.2478 μm) and 1-0 S(1) (2.1218 μm) line is often used to distinguish between the excitation mechanisms. The 2-1 S(1) / 1-0 S(1) ratio is predicted to be 0.53 – 0.56 for fluorescence (Black & Van Dishoeck, 1987) and 0.1 – 0.2 for excitation by shocks (Shull & Hollenbach, 1978). However, in dense PDRs (with a density close the lines' critical densities, which are 1.2 and 1.7 · 10^5 cm^{-3}) the low v levels are collisionally re-populated, thermalizing these low-energy levels. In this case the 2-1 S(1) / 1-0 S(1) decreases towards the typical values in the shock-regime with increasing density, complicating the analysis.

In our spectra we find strong evidence for UV fluorescence for all four sources (for cluster 1 UV fluorescence was already identified as an important excitation mechanism, Gilbert et al, 2000). In the H-band spectra various lines of very high vibrational levels, up to $v = 7$, are found. For example, the 5-3 O(3) line at 1.6135 μm is observed in all four sources. In case of pure UV fluorescence the relative strength of the this line compared to the 1-0 S(1) line is predicted to be 0.38 (Model 14, Black & Van Dishoeck, 1987). Since the excitation temperature of the 5-3 O(3) line is ~26,700K, the line strength would be 0.006 of the strength of the 1-0 S(1) line when excited thermally at 3000K. In that case, the 5-3 O(3) line would not be observable in our data.

The H_2 line ratios are listed in Table 4 (with the H_2 1-0 S(1) at 2.1218 μm as a reference line). Since the H_2 lines originate from the PDR, surrounding the H II region, the lines most probably suffer less extinction than derived from the hydrogen recombination lines. In Table 4 both the extinction-corrected (with A_V as calculated from the H I recombination lines, probably an overestimate for the extinction towards the H_2 lines) as the uncorrected (observed) values are given.

The high v levels ($v \geq 3$) originate exclusively from UV fluorescence. However, the observed v = 3,4,5,6,7 over 1-0 S(1) line ratios show lower values than predicted by models for pure UV excitation. This indicates that the 1-0 S(1) is (at least partly) thermalized, resulting in partial de-population of higher v-levels and thus boosted lower v-level populations. The thermalization of the $v = 1$ level emission lines is clear from the excitation diagrams as shown in Fig. 7 as well. In this figure the column density $N(v, j,)$ divided by the degeneracy g_J, is plotted as a function of the upper level energy $E(v, J)/k$.

$$\frac{N_{obs}(v, J)}{g_J} = \frac{4\pi\lambda}{hc}\frac{I_{obs}(v, J)}{A(v, J)} \tag{1}$$

$N_{obs}(v, J)$ is the observed column density for level (v, J), g_J is the level degeneracy, $A(v, J)$ the Einstein-A radiative transition probability (obtained from Wolniewicz et al, 1998), and $I_{obs}(v, J)$ is the observed, extinction-corrected line flux.

The $v = 1$ emission lines follow a thermal distribution (dashed line in the plots), while the higher v lines clearly deviate from it. The critical densities for the H_2 1-0 S(0), S(1), S(2), and S(3) lines range from 0.9 – 1.2 · 10^5 cm^{3}, so the density of the emitting gas has to be around or even above these values to be able to produce the observed line flux ratios. Inspection of the observed $v = 2$ line ratios (Table 4) reveals a trend in density; cluster 4 shows line ratios which are consistent with UV fluorescence, the $v = 2$ lines in cluster 1 are significantly thermalized, and cluster 2 and 3 are in between. The critical densities of the 2-1 S(1), S(2), and S(3) lines are 1.3 – 1.7 · 10^5 cm^{3}. So, cluster 1 has the highest molecular gas density, which is probably ≥ 1.5 · 10^5 cm^{3}. These densities are similar to the average molecular gas densities in ultra-compact H II regions on sub-parsec scales(Churchwell, 2002).

As expected, the plots in Fig. 7 are very similar to the excitation diagrams of dense PDRs (like the diagram for S140, Fig. 3 in Timmermann et al, 1996), showing clear differences from the smooth distribution expected for thermally excited H_2 lines (as for example in Fig. 5 of the shocked core in the Orion star-forming cloud, Rosenthal et al, 2000).

6. Conclusions

In this paper we presented medium-resolution near-IR spectroscopy of four very young star-forming regions in the overlap region of the merging Antennae galaxies. Clusters 1, 2 and 3 are very young (≤ 3 Myr) based on comparison of the EW(Brγ) with model predictions. In the K_s-band spectrum of cluster 4 CO bandheads can be found, indicating that this cluster is older, and approaches the red super giant phase. The age for this source as derived from the equivalent width of Brγ is 3 – 5 Myr.

The masses of cluster 1 and 2 are determined by scaling model SEDs of embedded star clusters to the K_s-band spectra. This results in a possible mass range of 1.1 – 1.2 · 10^6 $M_\odot$ for cluster 1 and 1.2 – 1.7 · 10^6 $M_\odot$ for cluster 2.

Table 4. Relative strength of low vibrational ($v \leq 3$) H_2 lines compared to H_2 1-0 S(1)..

Transition	$\lambda_{\rm rest}$ (μm)	UV[a]	thermal[b]	ratio cl1[c]	ratio cl2[c]	ratio cl3[c]	ratio cl4[c]
v = 1,2							
1-0 S(3)	1.9576	0.67	1.05	0.97 – 1.18	0.75 – 0.82	0.54 – 0.55	0.67 – 0.75
1-0 S(2)	2.0338	0.50	0.38	0.49 – 0.55	0.44 – 0.46	0.30 – 0.30	0.32 – 0.34
1-0 S(1)	2.1218	1.00	1.00	1.00 – 1.00	1.00 – 1.00	1.00 – 1.00	1.00 – 1.00
1-0 S(0)	2.2233	0.46	0.19	0.58 – 0.52	0.44 – 0.42	0.18 – 0.18	0.24 – 0.23
2-1 S(3)	2.0735	0.35	0.15	0.25 – 0.26	0.14 – 0.14	0.26 – 0.26	0.15 – 0.16
2-1 S(2)	2.1542	0.28	0.05	0.33 – 0.32	0.19 – 0.19	0.20 – 0.20	0.14 – 0.14
2-1 S(1)	2.2478	0.56	0.14	0.50 – 0.44	0.32 – 0.31	0.14 – 0.14	0.16 – 0.15
v = 3,4,5,6,7							
5-3 Q(1)	1.4929	0.43	<2.5e-5	0.07 – 0.22	0.10 – 0.17	0.16 – 0.17	0.04 – 0.08
5-3 Q(3)	1.5056	0.28	<2.5e-5	0.06 – 0.18	0.06 – 0.11	0.09 – 0.10	
4-2 O(3)	1.5099	0.42	<2.5e-5	0.08 – 0.24	0.07 – 0.11	0.11 – 0.12	0.05 – 0.09
6-4 Q(1)	1.6011	0.33	<2.5e-5	0.10 – 0.23	0.10 – 0.15		
5-3 O(3)	1.6135	0.38	<2.5e-5	0.09 – 0.20	0.09 – 0.14	0.19 – 0.20	0.06 – 0.10
7-5 S(1)	1.6206	0.20	<2.5e-5	0.03 – 0.06	0.04 – 0.06		
4-2 O(5)	1.6224	0.19	<2.5e-5	0.05 – 0.11	0.06 – 0.09		
7-5 Q(1)	1.7288	0.24	<2.5e-5	0.17 – 0.29	0.09 – 0.12		
6-4 O(3)	1.7326	0.31	<2.5e-5			0.05 – 0.05	0.07 – 0.10
3-2 S(1)	2.3864	0.29	0.02	0.23 – 0.19	0.19 – 0.17		

[a] Predicted line ratios for pure UV fluorescence (Model 14; Black & Van Dishoeck, 1987).

[b] Predicted line ratios for thermally excitated gas (T_{gas} = 3000K and $n_H = 10^5$ cm^{-3}). The ortho-para ratio is fixed at 3.

[c] Observed line ratios of H_2 X-X X(X) / H_2 1-0 S(1). Both the extinction-corrected and the uncorrected ratio values are listed (values range from uncorrected – extinction-corrected). The actual ratios most probably fall within this range, since the PDR from which the H_2 lines originate suffer less extinction than the H II regions (for which the values for A_V are calculated, see Table 1).

Numerous H_2 ro-vibrational lines are observed in the spectra, not only originating from the low vibrational levels ($v \leq 2$), but from high v levels as well, up to v = 7. This proves that UV fluorescence is an important excitation mechanism, since the gas temperatures required to excite these high v lines thermally are unrealistically high. Relative H_2 line strengths show that the lower v levels are (partly) thermalized, which is expected in dense PDRs. The derived molecular gas densities can be found in the range of several times 10^4 to 1.5 times 10^5 cm^{-3}.

The cluster at the region of most active star formation, cluster 1, corresponding to the brightest mid-IR peak discovered by ISO (Mirabel et al, 1998), and the highly reddened cluster 80 in HST images (Whitmore & Schweizer, 1995), has the densest molecular gas of all four clusters. In this source, the v = 2 ro-vibrational H_2 lines are significantly thermalized, indicating a gas density of $\geq 1.5 \cdot 10^5$ cm^{-3}.

Acknowledgements. We are very grateful to D. Jaffe, F. Israel, and E. Van Dishoeck for their valuable comments. Furthermore we thank the Paranal Observatory team for their support.

References

Brandl, B. R. et al, 2005, ApJ 635, 280
Black & Van Dishoeck
Churchwell, E., 2002, ARA&A 40, 27
Devillard, N., 1997, The Messenger 87, 19
Dopita, M. A., Kewley, L. J., Heisler, C. A. & Sutherland, R. S., 2000, ApJ 542, 224
Dopita, M. A., Groves, B. A., Sutherland, R. S., Binette, L. & Cecil, G., 2002, ApJ 572, 753
Draine, B. T., 1989, in ESLAB Symp. 22, IR Spectroscopy in Astronomy, ed. B. H. Kaldeich, ESA SP-290, 93
Fall, S. M., Chandar, R. & Whitmore, B. C., 2005, ApJ 631, 133
Förster Schreiber, N. M., Genzel, R., Lutz, D., Kunze, D. & Sternberg, A. 2001, ApJ 552, 544
Gao, Y. & Solomon, P., 2000, BAAS 197, 9603
Gilbert, A. M. et al, 2000, ApJ 533, 57
Gilbert, A. M. & Graham, J. R., 2007, accepted for publication in ApJ, arXiv:0706.3935v1
Groves, B. A., Dopita, M. A. & Sutherland, R. S., 2004, ApJS 153, 9
Hummer, D. G. & Storey, P. J., 1987, MNRAS, 224, 801
Leitherer C. et al, 1999, ApJS 123, 3
Lowe, R. P., Moorhead, J. M. & Wehlau, W. H., 1979, ApJ 228, 191
Martins, F., Schaerer, D. & Hillier, D. J., 2005, A&A 436, 1049
Mengel, S., Lehnert, M. D., Thatte, N., Tacconi-Garman, L. E. & Genzel, R., 2001, ApJ 550, 280
Mengel, S., Lehnert, M. D., Thatte, N. & Genzel, R., 2005, A&A 443, 41
Mihos, J. C., Bothun, G. D., & Richstone, D. O., 1993, ApJ 418, 82
Mirabel, I. F. et al 1998, A&A 333, L1
Moorwood A. et al, 1998, The Messenger 94, 7
Perryman, M. A. C. et al, 1997, A&A 323, 49
Rosenthal, D., Bertoldi, F. & Drapatz, S., 2000, A&A 356, 705
Shull & Hollenbach (from Burton)
Saviane, I., Hibbard, J. E. & Rich, M. R., 2004, AJ 127, 660
Snijders, L., Van der Werf, P. P., Brandl, B. R., Mengel, S., Schaerer, D. & Wang, Z., 2006, ApJ 648, 25
Snijders L., Kewley, L. J. & Van der Werf, P. P., 2007, in preparation
Sternberg, A., Hoffmann, T. L. & Pauldrach, A. W. A., 2003, ApJ 599, 1333
Sternberg, A. & Dalgarno, A., 1989, ApJ 338, 197
Timmermann, R., Bertoldi, F., Wright, C. M., Drapatz, S., Draine, B. T., Haser, L. & Sternberg, A., 1996, A&A 315, 281
Turner, J., Kirby-Docken, K. & Dalgarno, A., 1977, ApJS 35, 281
Vázquez, G. A. & Leitherer C., 2005, ApJ 621, 695
Vigroux, L. et al. 1996, A&A 315, L93
Whitmore, B. W. & Schweizer, F., 1995, AJ, 109, 960

Whitmore, B. C., Zhang, Q., Leitherer, C., Fall, M. S., Schweizer, F. & Miller, B. W., 1999, AJ 118, 1551
Wolniewicz, L., Simbotin, I. & Dalgarno A., 1998, ApJS 115, 293
Woosley, S. E., Langer, N. & Weaver, T. A., 1993, ApJ 411, 823

Table 2. Emission line fluxes

			Cluster 1		Cluster 2		Cluster 3		Cluster 4	
	Transition	$\lambda_{\rm rest}$ (μm)	$\lambda_{\rm obs}$ (μm)	Flux ± err (10^{-15} erg s^{-1} cm^{-2})	$\lambda_{\rm obs}$ (μm)	Flux ± err (10^{-15} erg s^{-1} cm^{-2})	$\lambda_{\rm obs}$ (μm)	Flux ± err (10^{-15} erg s^{-1} cm^{-2})	$\lambda_{\rm obs}$ (μm)	Flux ± err (10^{-15} erg s^{-1} cm^{-2})
Ionized hydrogen[a]										
H I	(5-3)	1.2822	1.2887	38.51 ± 4.22	1.2886	87.60 ± 5.24	1.2883	16.69 ± 1.53	1.2883	6.74 ± 0.64
H I	(30-4)	1.4852					1.4923	0.13 ± 0.01		
H I	(29-4)	1.4871	1.4947	0.10 ± 0.01	1.4945	0.21 ± 0.02	1.4942	0.17 ± 0.03		
H I	(28-4)	1.4892			1.4967	0.20 ± 0.01	1.4966	0.05 ± 0.01		
H I	(27-4)	1.4916	1.4992	0.08 ± 0.01	1.4990	0.23 ± 0.02	1.4986	0.12 ± 0.01		
H I	(25-4)	1.4971			1.5046	0.22 ± 0.02	1.5044	0.21 ± 0.03		
H I	(24-4)	1.5005	1.5082	0.14 ± 0.02	1.5081	0.27 ± 0.03				
H I	(23-4)	1.5041	1.5120	0.19 ± 0.01	1.5119	0.25 ± 0.03	1.5114	0.11 ± 0.01		
H I	(22-4)	1.5087	1.5164	0.27[c] ± 0.04	1.5163	0.48[c] ± 0.07	1.5159	0.33[c] ± 0.05		
H I	(21-4)	1.5137	1.5214	0.21 ± 0.02	1.5213	0.31 ± 0.03	1.5209	0.15 ± 0.02		
H I	(20-4)	1.5196	1.5274	0.22 ± 0.02	1.5272	0.39 ± 0.03	1.5268	0.23 ± 0.02		
H I	(19-4)	1.5265	1.5343	0.29 ± 0.03	1.5341	0.46 ± 0.05	1.5337	0.30 ± 0.05		
H I	(18-4)	1.5346	1.5425	0.37 ± 0.25	1.5423	0.61 ± 0.28	1.5419	0.37 ± 0.03	1.5417	0.16 ± 0.02
H I	(17-4)	1.5443	1.5522	0.50 ± 0.06	1.5521	0.74 ± 0.08	1.5518	0.62 ± 0.07		
H I	(16-4)	1.5561	1.5641	0.55 ± 0.14	1.5639	0.94 ± 0.10	1.5635	0.60 ± 0.05		
H I	(15-4)	1.5705	1.5785	0.70 ± 0.08	1.5784	1.05 ± 0.09	1.5779	0.70 ± 0.06	1.5777	0.15 ± 0.03
H I	(14-4)	1.5885	1.5966	0.83 ± 0.07	1.5965	1.29 ± 0.14	1.5960	0.82 ± 0.09	1.5959	0.21 ± 0.02
H I	(13-4)	1.6114	1.6196	0.98 ± 0.10	1.6194	1.60 ± 0.16	1.6190	0.99 ± 0.08	1.6188	0.30 ± 0.02
H I	(12-4)	1.6412	1.6496	1.52 ± 0.14	1.6494	2.01 ± 0.19	1.6489	1.33 ± 0.14	1.6488	0.83 ± 0.07
H I	(11-4)	1.6811	1.6895	2.37 ± 0.25	1.6894	3.22 ± 0.36	1.6891	1.74 ± 0.30	1.6889	1.26 ± 0.11
H I	(10-4)	1.7367	1.7453	3.30 ± 0.37	1.7451	4.58 ± 0.49	1.7449	3.13 ± 0.83	1.7446	1.76 ± 0.18
H I	(8-4)	1.9451	1.9552	9.41 ± 0.87	1.9551	12.86 ± 0.99	1.9545	1.73 ± 0.20	1.9544	2.08 ± 0.64
H I	(7-4)	2.1661	2.1772	14.02 ±1.55	2.1770	14.89 ± 1.59	2.1764	7.76 ± 1.70	2.1762	6.29 ± 0.79
			EW(Brγ) = 358 ± 36 Å		EW(Brγ) = 283 ± 28 Å		EW(Brγ) = 251 ± 25 Å		EW(Brγ) = 114 ± 11 Å	
Helium[a]										
HeI	3^3S-4^3P[d]	1.2531	1.2596	0.45 ± 0.04	1.2595	0.87 ± 0.09	1.2590	0.16 ± 0.01		
HeI	3^3D-3^3F[d]	1.2789	1.2854	1.73 ± 0.25	1.2853	3.79 ± 1.13	1.2850	0.53 ± 0.05	1.2850	0.32 ± 0.03
HeI	1^2D-1^3F	1.2794	1.2860	0.49 ± 0.08	1.2859	1.00 ± 0.37	1.2855	0.17 ± 0.02		
HeI	3^2P-3^1S[d]	1.4925					1.5000	0.23 ± 0.02		
HeI	1^3F-1^2D[d]	1.5876	1.5957	0.07 ± 0.01						
HeI	3^3D-3^*F[d]	1.6779	1.6863	0.06 ± 0.01						
HeI	1^3F-1^2D	1.6802								
HeI	3^3P-4^3D[d]	1.7007	1.7092	1.02 ± 0.15	1.7090	1.37 ± 0.15	1.7087	0.73 ± 0.08	1.7086	0.57 ± 0.05
HeI	1^2D-1^1P	1.7332			1.7418	0.05[f] ± 0.01			1.7410	0.38 ± 0.04
HeI	1^3F-1^2D[d]	1.7358					1.7439	0.28 ± 0.09		
HeI	1^1P-1^2D	1.7482					1.7564	0.54 ± 0.04		
HeI	3^3F-3^3D[d]	1.9443	1.9540	0.57 ± 0.09	1.9540	0.55 ± 0.19	1.9539	1.56 ± 0.44	1.9539	2.63 ± 0.57
HeI	3^3P-3^2D[d]	1.9548					1.9642	0.53 ± 0.05		
HeI	2^1S-2^1P[d]	2.0587	2.0692	9.00 ± 0.79	2.0691	9.08 ± 0.80	2.0684	4.08 ± 0.39	2.0683	2.74 ± 0.26
HeI	3^2P-4^1S[d]	2.1127	2.1235	0.40 ± 0.03	2.1233	0.38 ± 0.05				
HeI	3^3D-3^4F[d]	2.1614	2.1726	0.45 ± 0.05	2.1723	0.40 ± 0.04				
HeI	3^3G-3^3F[d]	2.1647	2.1758	0.69 ± 0.08			2.1749	0.36 ± 0.04	2.1746	
HeI	1^1P-1^2D	2.1847					2.1956	0.18 ± 0.03		

Molecular hydrogen[b]										
H_2	2-0 Q(3)	1.2473							1.2533	0.10 ± 0.02
H_2	5-3 Q(1)	1.4929	1.5006	0.11 ± 0.02	1.5004	0.18 ± 0.02	1.5000	0.23 ± 0.02	1.5001	0.20 ± 0.04
H_2	5-3 Q(3)	1.5056			1.5132	0.11 ± 0.01	1.5128	0.15 ± 0.03	1.5129	0.17 ± 0.01
H_2	4-2 O(3)	1.5099	1.5176	0.13 ± 0.02	1.5174	0.13 ± 0.02	1.5171	0.16 ± 0.02	1.5170	0.23 ± 0.02
H_2	6-4 Q(1)	1.6011	1.6098	0.18 ± 0.02	1.6096	0.14 ± 0.01	1.6092	0.24 ± 0.02	1.6092	0.28 ± 0.03
H_2	5-3 O(3)	1.6135	1.6218	0.17 ± 0.02	1.6217	0.22 ± 0.02	1.6213	0.22 ± 0.02	1.6212	0.24 ± 0.03
H_2	7-5 S(1)	1.6206					1.6283	0.10 ± 0.02	1.6282	0.08 ± 0.01
H_2	4-2 O(5)	1.6224					1.6302	0.14 ± 0.04	1.6300	0.14 ± 0.02
H_2	7-5 Q(1)	1.7288					1.7371	0.22 ± 0.03	1.7371	0.46 ± 0.05
H_2	6-4 O(3)	1.7326	1.7412	0.20[e] ± 0.02	1.7412	0.06 ± 0.01				
H_2	1-0 S(7)	1.7480							1.7564	0.68 ± 0.06
H_2	1-0 S(3)	1.9576	1.9679	1.82 ± 0.20	1.9676	0.63 ± 0.05	1.9670	1.74 ± 0.14	1.9670	2.66 ± 0.22
H_2	1-0 S(2)	2.0338	2.0443	0.88 ± 0.08	2.0440	0.35 ± 0.03	2.0436	1.02 ± 0.11	2.0435	1.35 ± 0.15
H_2	2-1 S(3)	2.0735	2.0842	0.42 ± 0.04	2.0839	0.30 ± 0.03	2.0834	0.32 ± 0.05	2.0834	0.67 ± 0.09
H_2	1-0 S(1)	2.1218	2.1329	2.73 ± 0.25	2.1326	1.16 ± 0.09	2.1321	2.32 ± 0.23	2.1320	2.73 ± 0.24
H_2	2-1 S(2)	2.1542	2.1654	0.39 ± 0.05	2.1652	0.23 ± 0.02	2.1646	0.44 ± 0.05	2.1644	0.90 ± 0.08
H_2	1-0 S(0)	2.2233	2.2347	0.66 ± 0.07	2.2345	0.21 ± 0.02	2.2340	1.03 ± 0.13	2.2340	1.57 ± 0.14
H_2	2-1 S(1)	2.2478	2.2592	0.64 ± 0.07	2.2586	0.16 ± 0.02	2.2586	0.75 ± 0.05	2.2585	1.37 ± 0.14
H_2	3-2 S(1)	2.3864					2.3975	0.45 ± 0.04	2.3975	0.64 ± 0.05
H_2	1-0 Q(1)	2.4066					2.4177	2.46 ± 0.19	2.4177	3.02 ± 0.33
H_2	1-0 Q(2)	2.4134					2.4246	1.38 ± 0.17	2.4246	1.91 ± 0.17
H_2	1-0 Q(3)	2.4237							2.4360	1.18 ± 0.14
H_2	1-0 Q(4)	2.4375					2.4486	0.47 ± 0.04	2.4488	1.07 ± 0.09
H_2	1-0 Q(5)	2.4548					2.4661	0.78 ± 0.08	2.4660	1.16 ± 0.08
Iron[b]										
[FeII]	$a^6D_{9/2}$-$a^4D_{7/2}$	1.2572	1.2635	3.23 ± 0.28	1.2634	5.94 ± 0.42	1.2631	1.43 ± 0.14	1.2631	1.56 ± 0.15
[FeII]	$a^4F_{9/2}$-$a^4D_{5/2}$	1.5339	1.5417	0.22 ± 0.38	1.5416	0.29 ± 0.06	1.5412	0.14 ± 0.04		
[FeII]	$a^4F_{7/2}$-$a^4D_{3/2}$	1.5999					1.6077	0.16 ± 0.03		
[FeII]	$a^4G_{9/2}$-$b^2F_{7/2}$	1.6145							1.6223	0.08 ± 0.01
[FeII]	$a^4F_{9/2}$-$a^4D_{7/2}$	1.6440	1.6524	2.87 ± 0.23	1.6522	3.59 ± 0.39	1.6518	3.05 ± 0.35	1.6518	5.34 ± 0.52
[FeII]	$a^2G_{9/2}$-$a^4H_{7/2}$	1.7044					1.7122	0.10 ± 0.02		
[FeII]	$a^2P_{3/2}$-$b^4F_{3/2}$	2.1410							2.1509	0.12 ± 0.01
[FeIII]	$^3G_5$-$^3H_6$	2.2184	2.2300	0.32 ± 0.04	2.2299	0.43 ± 0.03				

[a] Linefluxes measured in a 3.″5 aperture.

[b] Linefluxes measured in a 5.″1 aperture to take extended emission of molecular hydrogen and iron into account.

[c] Flux unreliable due to feature in standard star spectrum.

[d] Possible blend of several helium lines.

[e] Possible blend with HeI 1^2D-1^1P .

[f] Possible blend with H_2 6-4 O(3).